Geophysical Research Letters

RESEARCH LETTER
10.1029/2018GL081858

Wave Activity in Jupiter's North Equatorial Belt From Near-Infrared Reflectivity Observations

Rohini S. Giles[1], Glenn S. Orton[1], Andrew W. Stephens[2], Michael H. Wong[3], Patrick G. J. Irwin[4], James A. Sinclair[1], and Fachreddin Tabataba-Vakili[1]

[1]Jet Propulsion Laboratory, California Institute of Technology, Pasadena, CA, USA, [2]Gemini Observatory, Hilo, HI, USA, [3]Astronomy Department, University of California, Berkeley, Berkeley, CA, USA, [4]Atmospheric, Oceanic and Planetary Physics, Department of Physics, University of Oxford, Oxford, UK

Key Points:
- Near-infrared images of Jupiter are used to track the evolution of a wave pattern in the planet's North Equatorial Belt
- The wave pattern has a wave number of ~18, is located at 12–17°N, and moves slowly westward
- The bright and dark regions of the wave are caused by variations in the vertical location of the upper tropospheric haze layer

Supporting Information:
- Supporting Information S1

Correspondence to:
R. S. Giles,
rohini.s.giles@jpl.nasa.gov

Citation:
Giles, R. S., Orton, G. S., Stephens, A. W., Wong, M. H., Irwin, P. G., Sinclair, J. A., & Tabataba-Vakili, F. (2019). Wave activity in Jupiter's North Equatorial Belt from near-infrared reflectivity observations. *Geophysical Research Letters*, *46*, 1232–1241. https://doi.org/10.1029/2018GL081858

Received 27 DEC 2018
Accepted 31 JAN 2019
Accepted article online 5 FEB 2019
Published online 13 FEB 2019

Abstract High spatial resolution images of Jupiter at 1.58–2.28 μm are used to track and characterize a wave pattern observed in 2017 at a planetocentric latitude of 14°N. The wave pattern has a wave number of 18 and spans ~5° in latitude. One bright crest remains stationary in System III longitude, while the remaining crests move slowly westward. The bright and dark regions of the near-infrared wave pattern are caused by variations in the vertical location of the upper tropospheric haze layer. A comparison with thermal infrared observations shows a correlation with temperature anomalies in the upper troposphere. The results are consistent with a Rossby wave, generated by flow around a stationary vortex.

Plain Language Summary The Gemini North telescope was used to take high spatial resolution images of Jupiter in the near-infrared during 2017–2018. These images can be used to track the complex movement of hazes in Jupiter's upper atmosphere. The timing of these observations is particularly relevant because the Juno mission is currently in orbit around Jupiter, and near-infrared images of the entire planet's disk can be used to place the measurements from Juno's instruments in a broader context. In this paper, we focus on a particularly prominent atmospheric feature that was observed during this time period: a bright wave pattern in Jupiter's northern hemisphere. We track the movement of this wave pattern with time, we study its three-dimensional structure, and we compare these near-infrared observations with images taken in the visible and thermal infrared. We find that the wave is consistent with a Rossby wave, generated by flow around a stationary vortex. These results can be used to inform future numerical simulations of Jupiter's atmosphere, helping us to understand the dynamics that drive the planet's complex weather patterns.

1. Introduction

Jupiter's complex atmospheric circulation leads to some of the most dramatic weather in the solar system, including long-lived vortices (Hatzes et al., 1981), large-scale convective storms (Hueso et al., 2002), and periodic global upheavals that temporarily change the banded appearance of the planet (Fletcher et al., 2011). One region of the planet that has exhibited significant temporal variability in the past is the North Equatorial Belt (NEB), which has periodically shown strong large-scale wave patterns that extend across large longitude ranges (e.g., Magalhaes et al., 1989).

The NEB is a red-colored belt in Jupiter's cloudy, convective weather layer, lying immediately to the north of the planet's pale-colored Equatorial Zone. As delimited by its coloration and albedo, the belt typically spans the 6.4–15.7°N latitude range (Rogers, 1995; all latitudes quoted in this paper are planetocentric), although there are periods in time when it temporarily extends several degrees further north, a phenomenon known as an expansion event (Fletcher et al., 2017; Rogers, 1995). The typical extent of the NEB coincides with a band of cyclonic shear in the zonal wind field, bounded to the north by a westward jet peaking in the 15–16°N range, and to the south by an eastward jet peaking in the 4–8°N range (Johnson et al., 2018; Tollefson et al., 2017). Further to the north, the belt/zone patterns of cloud color and albedo lose their tight association with cyclonic and anticyclonic shear in the zonal wind field (Limaye, 1986), but the upper tropospheric haze distribution continues to track the zonal wind shear (Wong et al., 2008). In this paper, we use the term NEB to describe both the reddish belt at cloud level, and the overlying upper tropospheric layer characterized by low haze reflectivity and cyclonic wind shear.

Upper-tropospheric, planetary-scale waves in the NEB have been observed by both spacecraft (Li et al., 2006; Magalhaes et al., 1989) and ground-based observations (Deming et al., 1989; Fisher et al., 2016; Fletcher et al., 2017; Orton et al., 1994; Rogers et al., 2004). The majority of these observations have been made in the thermal infrared, and the wave pattern manifests as a series of warm and cool temperature anomalies in the upper troposphere. In addition, NEB waves have been observed in near-ultraviolet and near-infrared methane-band images, both of which are sensitive to Jupiter's upper tropospheric (0.1–0.6 bar) haze layer (Li et al., 2006; Rogers et al., 2004). There is significant temporal variability in the appearance of the NEB waves; there are periods of time where no waves are observed at all, and when they are present, their wave numbers can vary between 9 (Magalhaes et al., 1989) and 17 (Fletcher et al., 2017). The cause of the temporal variability is not well understood, although Fletcher et al. (2017) have suggested that the presence of waves could be related to the periodic expansion events.

Since the Juno spacecraft entered into orbit around Jupiter in July 2016, there has been an extensive campaign of ground-based supporting observations. One important component of that campaign is an ongoing series of near-infrared images of Jupiter made with the Near-Infrared Imager (NIRI) at the Gemini North telescope (Hodapp et al., 2003). These high spatial resolution images are sensitive to the clouds and hazes in Jupiter's upper troposphere (0.1–0.6 bar), and they supplement the spatial, spectral, and temporal coverage provided by the mission's instruments. In addition to supporting the mission, this data set provides a valuable tool in tracking Jupiter's constantly changing weather patterns.

In the first year of the Juno observations, Jupiter's NEB underwent a periodic expansion event (Fletcher et al., 2018), which coincided with a period of extensive NEB wave activity in the upper troposphere. In this paper, we use the 1.58–2.28 μm observations of Jupiter made by NIRI to study these waves. This is the first time that a time series of NEB waves at these wavelengths has been published. The high frequency of observations allows us to track individual wave crests with time (section 3), and by combining multiple filters in the near infrared, we are able to measure the three-dimensional distribution of aerosols in Jupiter's upper troposphere (section 4). In section 5, we discuss the near-infrared results and compare them with observations made in the visible and thermal infrared.

2. Observations

2.1. NIRI Observations

In 2017–2018, the NIRI instrument at the Gemini North telescope was used to take a series of high spatial resolution observations of Jupiter, using adaptive-optics stabilization. We used a set of six filters, centered at 1.58, 1.69, 2.05, 2.17, 2.25, and 2.28 μm, which together probe the 0.1–0.6 bar pressure range in Jupiter's upper troposphere. The f/14 camera was used, which provides a $51'' \times 51''$ field of view that is large enough to simultaneously observe the entire planetary disk. The Gemini adaptive optics system (ALTAIR) used the closest Galilean satellite as a natural guide star for wavefront correction. The requirement to have a satellite visible within the field of view for the duration of the 30-min observation sequence places limitations on the timings of the observations. By using ALTAIR, we obtain a final spatial resolution of $\sim 0.1''$.

NIRI observations of Jupiter were made on 18 dates between January 2017 and July 2018. Where possible, observations were timed to coincide with the dates and/or longitudes of the Juno mission perijoves. Observations of the faint standard star GSPC S791-C were made for a subset of the observing dates.

2.2. Data Reduction

The NIRI images were initially reduced using the Gemini IRAF package. Images were then sky subtracted, flat fielded, and finally coadded using a bad pixel mask. The same process was applied to observations of the standard star.

The images obtained on the same night as a standard star observation were then radiometrically calibrated. The jovian calibration factor was calculated from the ratio of the stellar irradiance and the observed stellar counts, taking into account the differences in integration time and airmass, and dividing by the solid angle subtended by each pixel. The observed stellar counts and associated error were obtained using the IRAF *phot* package. The reference stellar irradiance (and associated error) of star GSPC S791-C in each filter was obtained by fitting a black-body curve to the JHK data from Leggett et al. (2006). The error on the calibration is dominated by the sky noise relative to stellar counts in the stellar images, and varies between ~15% for the

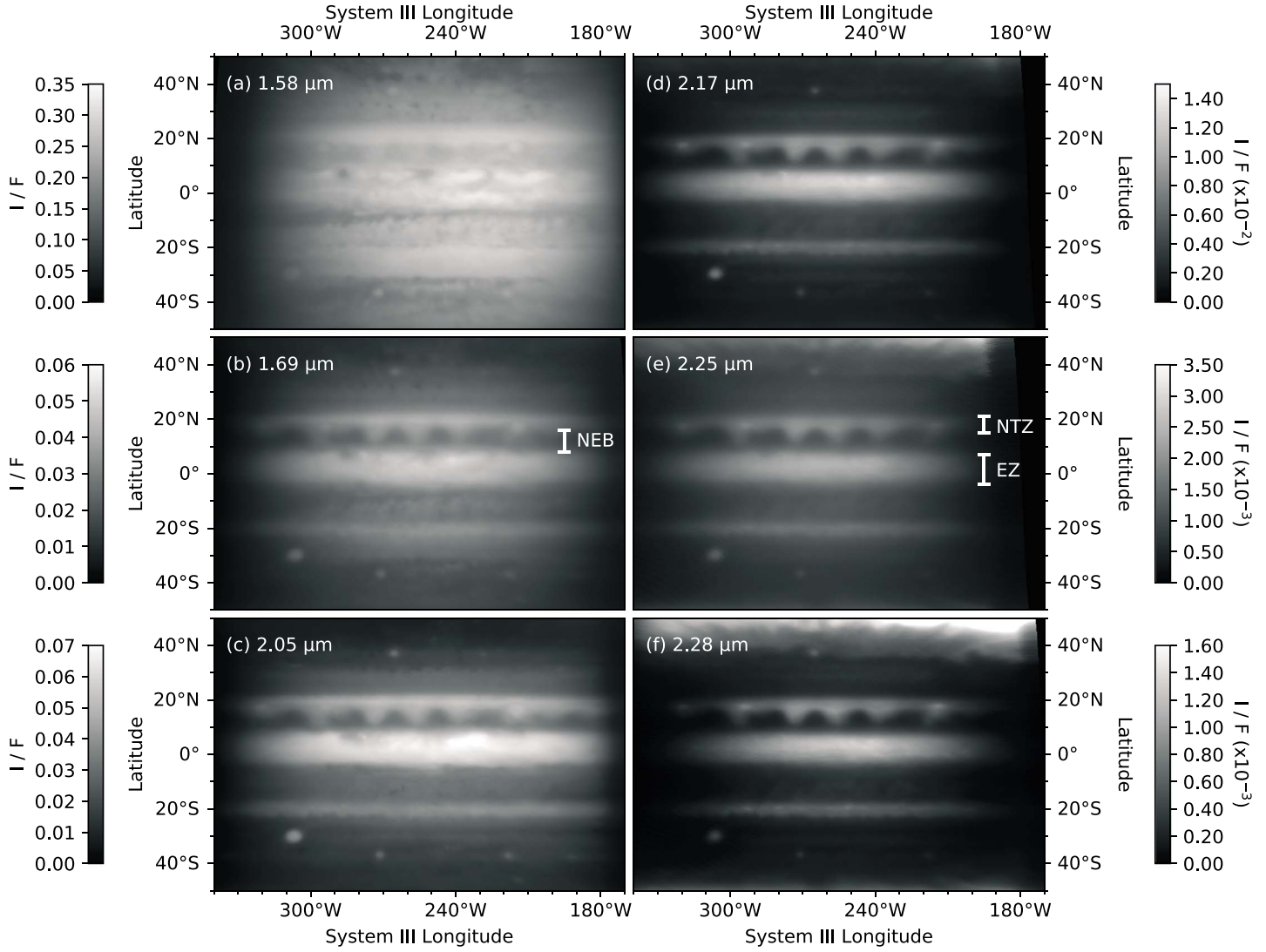

Figure 1. Near-Infrared Imager adaptive-optics images of Jupiter from 29 June 2017. Observations were made in six filters between 1.58 and 2.28 μm. A prominent wave feature can be seen in the planet's North Equatorial Belt (NEB).

filter with least noise and ~75% for the noisiest filter (the stellar counts are lower in the longer-wavelength filters).

For each date, images were geometrically calibrated by visually fitting the planet's limb, in order to assign latitudes, longitudes, and viewing angle geometries. The cylindrically projected images from each filter were then stacked together in order to form an image cube consisting of six-point spectra. An example of the fully reduced near-infrared images from 29 June 2017 is shown in Figure 1. The latitudes corresponding to the Equatorial Zone (EZ), North Equatorial Belt (NEB), and North Tropical Zone (NTZ) are labeled. Figures S1 and S2 in the supporting information show midinfrared and visible-light images of Jupiter for comparison.

The six images shown in Figure 1 are each sensitive to a slightly different region of the upper troposphere. Within the relatively haze-free NEB, the following pressure levels are probed by each filter: 0.25–0.69 bar at 1.58 μm, 0.20–0.44 bar at 1.69 μm, 0.20–0.43 bar at 2.05 μm, 0.16–0.35 bar at 2.17 μm, 0.13–0.31 bar at 2.25 μm, and 0.13–0.32 bar at 2.28 μm. In regions of the planet with a higher concentration of haze particles, slightly lower pressures will be probed.

The set of observations presented in Figure 1 shows a prominent wave feature in Jupiter's dark NEB, at the belt's boundary with the bright haze band over the NTZ. This wave feature and its evolution with time are the focus of this study.

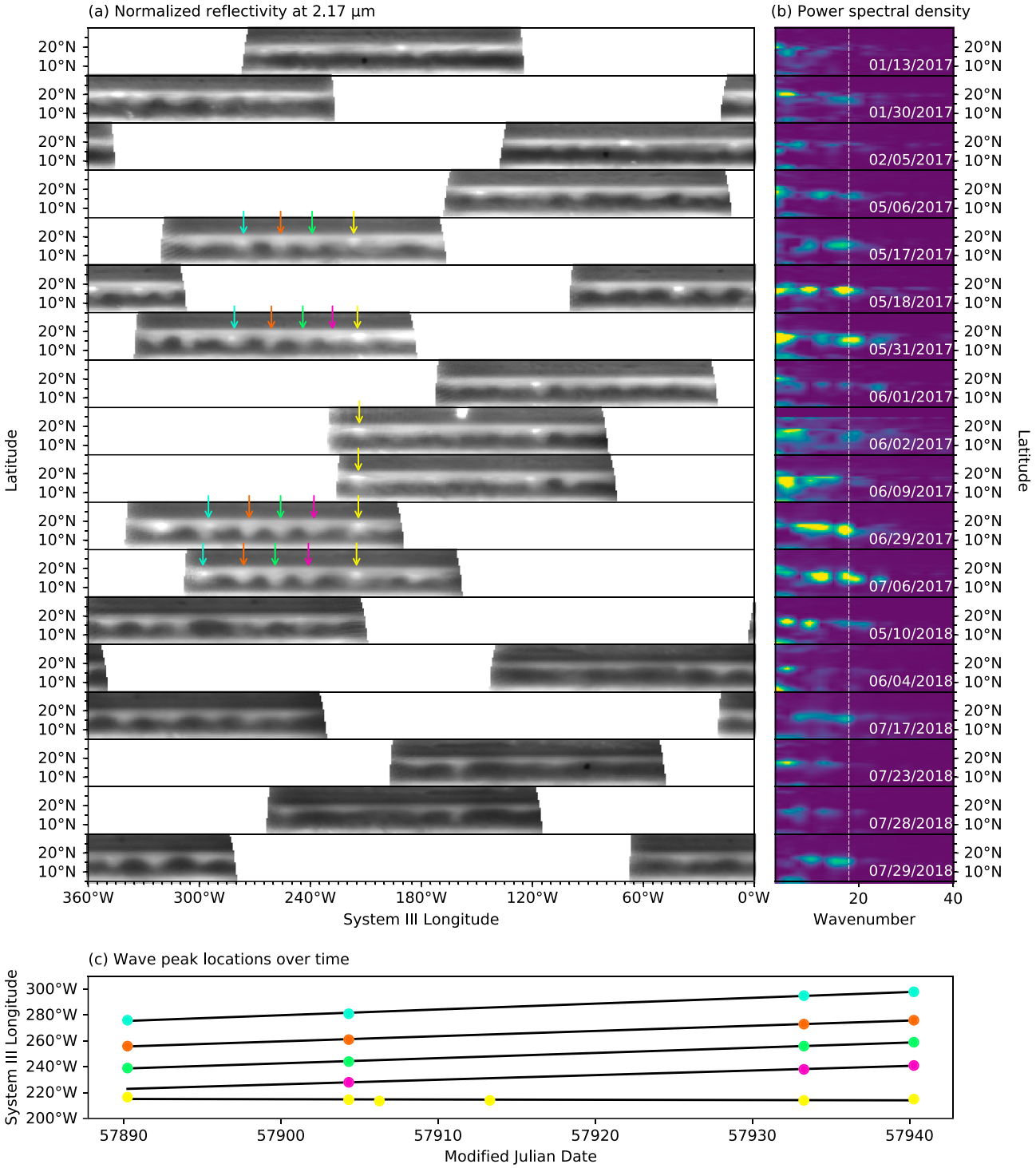

Figure 2. (a) The 2.17-μm images of wave features in Jupiter's North Equatorial Belt between January 2017 and July 2018. Wave crests are highlighted by colored arrows. (b) The power spectral density at each latitude point, with the wave number of 18 highlighted by the white dashed line. (c) The location of each wave crest as a function of time (MJD 57890 is 17 May 2017). MJD = Modified Julian Date.

3. Wave Morphology

Figure 2a shows Jupiter's dark NEB and bright NTZ at 2.17 μm for each of the 18 observing dates between January 2017 and July 2018. The images have been modified to correct for limb darkening by fitting the Minnaert function (Minnaert, 1941) at each latitude band and have been normalized by dividing by the average equatorial radiance (which is assumed to be constant during this time period). This series of images shows the evolution of the NEB wave pattern that is seen in Figure 1. Figure 2b shows the power spectral density at each latitude, where bright regions highlight the wave numbers of the strongest wave components.

The wave features are most apparent in May–July 2017; they are not seen in January 2017, and while there are some crests visible in the 2018 images, the amplitude is lower than in spring/summer 2017. Throughout this time period, the wave pattern is located between latitudes of 12°N and 17°N and is strongest at longitudes of 200°W–360°W. Measurement of the average spacing between the bright wave crests shows that the wave number of the NEB wave is ~18; this is further shown by Figure 2b, which shows a strong component at ~18. This wave number corresponds to a wavelength of 24,000 km at the 300-mbar pressure level.

We were able to track individual wave crests between 17 May 2017 and 6 July 2017. These wave crests are marked by the colored arrows in Figure 2a and their longitudinal positions as a function of time are shown in Figure 2c (using the same colors). The uncertainty in each wave crest position is ~1°. The westward drift rates of each wave crest, in degrees per day, are as follows: 0.45 ± 0.02 (blue), 0.40 ± 0.01 (orange), 0.40 ± 0.01 (green), 0.36 ± 0.01 (pink), and -0.02 ± 0.03 (yellow).

The crest marked by the yellow arrow appears to be unique, as it remains approximately stationary with respect to the System III Longitude system. The remaining marked crests drift westward away from this stationary crest. We initially observe three moving wave crests, but an additional crest forms between 17 and 31 May (marked by the pink arrow) and then also moves wesward. We note that the closer the moving crests are located to the stationary crest, the slower their measured westward drift rate. However, it is unclear whether these differences in phase speed are statistically significant; if genuine, it could be caused by longitudinal variations in the background zonal flow (Johnson et al., 2018). The four moving wave crests have an average phase speed of 0.39 ± 0.01°/day, which corresponds to a speed of 5.44 ± 0.14 m/s at the 300-mbar level. Applying the thermal wind equation to Cassini CIRS data has shown that the zonal wind at 500 mbar is between ~2 m/s westward and ~20 m/s eastward at 12–16°N (Li et al., 2006).

4. Tropospheric Haze Distribution

4.1. Spectral Modeling

In order to provide constraints on the vertical profile of the aerosol opacity, the six-point NIRI spectra were analyzed using the NEMESIS radiative transfer and retrieval tool (Irwin et al., 2008). NEMESIS uses a multiple-scattering radiative transfer code to calculate a synthetic spectrum for a given atmospheric model, making use of the correlated-*k* approximation (Lacis & Oinas, 1991) to improve its efficiency. The atmospheric model is then iteratively adjusted to fit the observed spectrum, following an optimal estimation technique.

The atmospheric model consists of 39 layers (the maximum allowed by NEMESIS) between 6 bar and 10 mbar, equally spaced in log(p), and the pressure-temperature profile is taken from Cassini CIRS observations (Fletcher et al., 2009). H_2 and He are assumed to have well-mixed volume mixing ratios of 0.863 and 0.134, respectively (Niemann et al., 1998), the vertical profiles of NH_3 and PH_3 are taken from Fletcher et al. (2009), and the vertical profiles CH_4 and C_2H_2 are obtained from Nixon et al. (2007). Molecular line data was obtained from HITRAN 2016 (Gordon et al., 2017) and was used to generate channel-integrated *k*-tables for each NIRI filter. Collision-induced absorption data were obtained from Orton et al. (2007) and Borysow et al. (1988).

In this section, we focus on the observations from 29 June 2017, shown in Figure 1. This date corresponds to the peak amplitude of the observed NEB wave pattern and also belongs to the subset of dates when the standard star was also observed, allowing the images to be radiometrically calibrated. The six-point NIRI spectra are primarily sensitive to Jupiter's upper tropospheric clouds and hazes. We therefore hold the gaseous abundances fixed at their a priori values during the NEMESIS retrievals and only allow the haze properties to vary. Section 4.2 describes the initial retrieval of the aerosol's imaginary refractive index from Equatorial Zone data. In section 4.3, this aerosol model is then used to retrieve the vertical opacity profile in the NEB.

4.2. Retrieval of Aerosol Scattering Properties

The absorption and scattering properties of the aerosol particles have a significant impact on the radiative transfer modeling of the atmosphere. Before running retrievals of the haze opacity in the highly variable NEB wave region, we therefore used observations of the bright and relatively homogeneous EZ to produce an appropriate aerosol model.

Unlike the NEB wave region, the EZ did not exhibit any significant variability in brightness in the 29 June 2017 data set. Because of this, we made the assumption that there is no longitudinal variability in the haze structure, which in turn means that observations from different longitudes can be considered to be different viewing geometries of the same haze layer. Observations from the central part of the EZ (1.25°S–4.5°N) were binned according to emission angle and solar zenith angle, using 5°-wide bins. There were 57 bins which contained observations from all six filters; the observations from each of these bins were averaged to produce a final set of 57 six-point spectra.

These 57 spectra were then used to simultaneously retrieve the complex refractive index spectrum for the aerosol; the complex refractive index governs the extinction cross section, the single-scattering albedo and the phase function, all of which are used in the radiative transfer model. This retrieval requires a reference value for the real refractive index at a given wavelength; we used 1.4 at 2.0 μm, which is the value for NH_3 ice given by Martonchik et al. (1984). In order to avoid additional degeneracies in the retrieval, we assume that the aerosol particles have a radius of 0.75 $\pm$ 0.05 μm, which is consistent with observations from both the Galileo near-infrared mapping spectrometer (Irwin et al., 1998) and the Galileo probe net flux radiometer (Sromovsky et al., 1998). We retrieve the complex refractive index spectrum at intervals of 0.025 μm between 1.550 and 2.325 μm and assume a correlation length of 2 to ensure that the spectrum is relatively smooth. In addition to retrieving the complex refractive index, we also retrieved the vertical location and maximum particle density of the haze layer, assuming a Gaussian shape in log(p) space with a width of 0.8. A simple Gaussian shape was chosen to prevent overfitting the six-point spectra, and the width of 0.8 was the average value obtained during a preliminary analysis in which the width was also allowed to vary.

The resulting best fit haze model for the EZ is centered at a pressure level of 360 mbar and a total optical thickness of 9 at 2.0 μm. The retrieved imaginary refractive index spectrum does show a peak at ~2.3 μm, which is qualitatively similar in behavior to NH_3 ice (Martonchik et al., 1984), although the retrieved values are a factor of 10 higher (~0.01–0.1). This results in a single-scattering albedo that varies between 0.97 at 1.6 μm and 0.34 at 2.3 μm. However, it should be cautioned that due to the very limited number of spectral points in this data set, and the degeneracies between the real refractive index, imaginary refractive index, and particle size distribution, it is not feasible to draw meaningful conclusions from the results of the complex refractive index retrieval; instead, the purpose of this exercise is simply to produce an aerosol model that can accurately fit the EZ data and can be extrapolated to the NEB.

4.3. Retrievals of Three-Dimensional Aerosol Opacity

We now turn to the primary goal of this section: the retrieval of the NEB aerosol distribution for the 29 June 2017 data set. The six images shown in Figure 1 were stacked together to form an image cube, and retrievals were run for each longitude and latitude point. We assume that the haze layer has a Gaussian shape, and we retrieve the peak pressure level, peak particle density, and width. The imaginary refractive index spectrum was taken from the results of the previous section and was held fixed.

The results from these retrievals are shown in Figure 3. Figure 3a shows the reflecitvity at 2.17 μm and is simply a reproduction of Figure 1d, shown for comparison purposes. Figure 3b shows the total optical thickness of the haze layer for the same longitude and latitude range as Figure 3a. Finally, Figure 3c shows a slice through the three-dimensional aerosol specific density distribution at a latitude of 14°N; this latitude is in the center of the wave and is marked in Figures 3a and 3b by the white dashed line.

Figure 3c shows that there is a clear relationship between the crests and troughs of the wave seen in Figure 3a and the location of the upper tropospheric haze. In the bright crests, the haze layer is located higher in the atmosphere, at a pressure level of ~280 mbar. In the dark troughs, the haze is located deeper in the atmosphere, at a pressure of ~350 mbar. In contrast, Figure 3b shows that there is not a strong correlation between the crests/troughs and regions of high/low total optical thickness. The NTZ, which is immediately north of the NEB and is bright in the reflected sunlight image, has a consistently higher optical thickness than the NEB. However, the wave crests in the NEB, despite having a similar brightness to the NTZ, appear

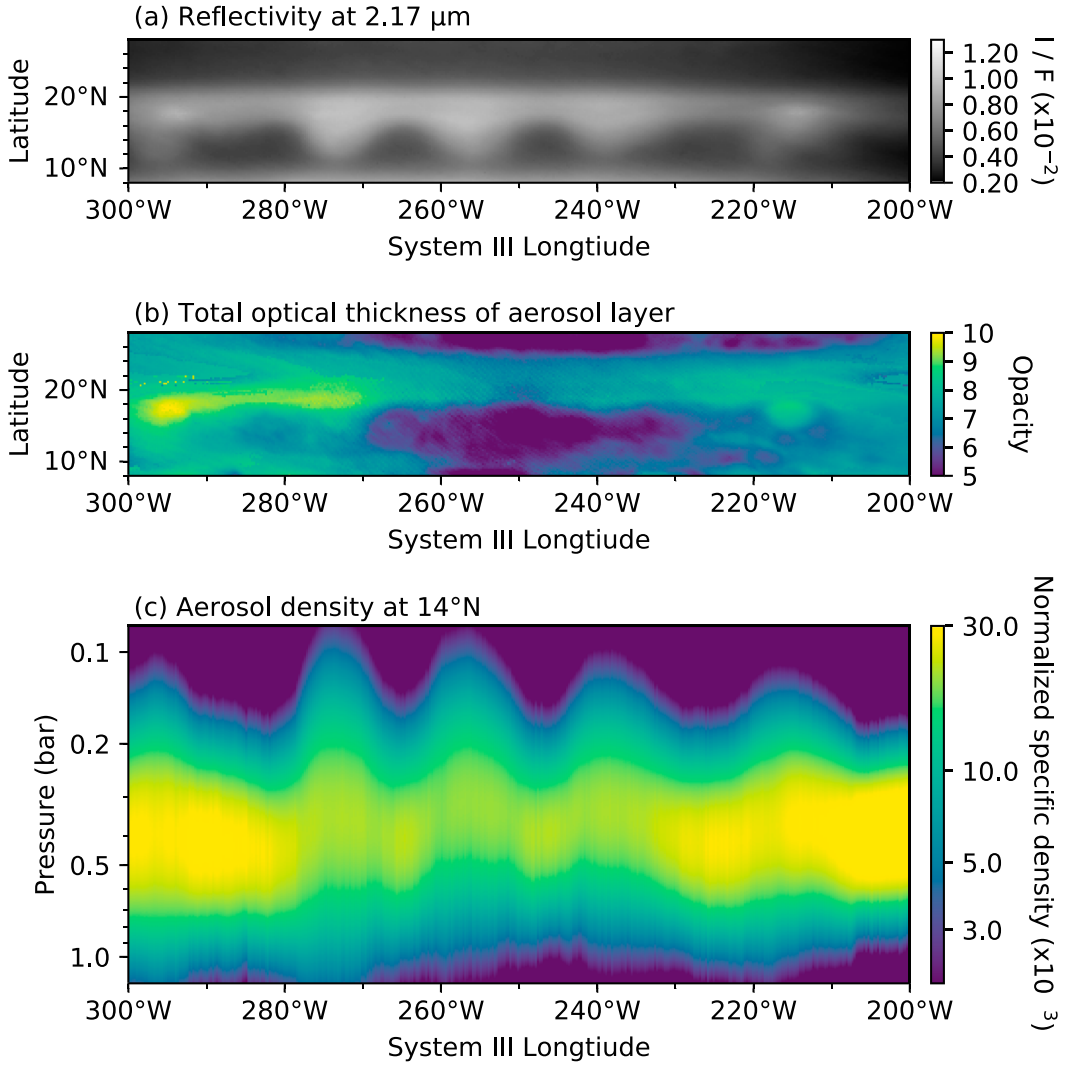

Figure 3. Retrievals of aerosol opacity from 29 June 2017 images of the North Equatorial Belt wave. (a) Image of the wave pattern at 2.17 μm image, as seen in Figure 1. (b) Total optical thickness of the retrieved upper tropospheric aerosol layer. (c) The specific density (particles/gram) of the aerosol as a function of pressure, at a latitude of 14°N (marked by dashed white lines in (a) and (b)). The specific density has been normalized by assuming that the particles have a cross section of 1 cm^2.

to have the same low total opacity as the dark troughs. The near-infrared wave pattern therefore reveals variations in the location of the haze layer, rather than differences in the total optical thickness of the haze.

One exception to this overall trend is the stationary crest at 215°W. Figure 2 shows that this crest is unique because it remains fixed in System III longitude, and Figure 3b shows it also has an unusual opacity distribution; unlike the adjacent westward moving crests, it corresponds to a discrete, circular region of high total optical thickness. This crest corresponds to a long-lived feature known as White Spot Z and is discussed further in section 5.

5. Discussion and Conclusions

In this study, we used near-infrared images of Jupiter to track and characterize a prominent wave feature in the planet's North Equatorial Belt in May–July 2017. The results of this analysis are summarized below.

1. The wave pattern is located at latitudes of 12–17°N (planetocentric).
2. The wave number is ~18, which corresponds to a wavelength of 24,000 km.
3. The majority of the crests move to the west (relative to System III) with a phase speed of 5.44 ± 0.14 m/s.

4. The wave crest that marks the eastern boundary of the wave pattern stays fixed in System III longitude.
5. The observed differences in brightness between the wave crests and troughs are primarily driven by variations in the aerosol location. The haze layer is located higher in the atmosphere (~280 mbar) in the bright crests and lower in the atmosphere (~350 mbar) in the dark troughs.

In addition to these observations in the near infrared, the extensive Juno support campaign means that there have been many images taken of Jupiter during this time period at other wavelengths. Simon et al. (2018) and Fletcher et al. (2018) studied mesoscale waves in Jupiter's NEB in 2016–2017 using visible and 5-μm images, respectively. These mesoscale waves have a much smaller wavelength (1,300–1,600 km) than the NEB wave pattern described in this paper, but both studies suggested that the origin of the small-scale waves could be related to a series of cyclone-anticylone pairs that they observed in the NEB; these vortices appear to be correlated with the near-infrared wave pattern presented in this paper. The cyclone-anticyclone pattern described in Fletcher et al. (2018) was observed in both the 5-μm images and visible-light images from the Hubble Space Telescope. The cyclones were first observed in February 2017 and the anticyclones had formed by March 2017. The cyclones and anticyclones were observed at planetocentric latitudes of 14°N and 17°N, respectively, were restricted to longitudes of 250–340°W, and had a wave number of ~16. These properties are all similar to the near-infrared wave, but the time gap between observations makes it difficult to conclusively tie them together. However, (Simon et al., 2018) presents visible-light observations from the Pic du Midi observatory in June 2017, which coincides with the near-infrared NIRI observations. These visible-light observations show two prominent anticyclones which match the locations of two of the bright near-infrared crests, highlighted by the yellow and blue markers in Figure 2; there are no anticylones seen at the locations of the other two crests.

In addition to the visible light and 5-μm observations that were made contemporaneously with the NIRI near-infrared observations, Fletcher et al. (2017) also measured a NEB wave pattern in thermal infrared images in early 2016. These observations are sensitive to Jupiter's temperature profile and show an alternating pattern of warm and cool regions in the upper troposphere (<500 mbar). Despite the fact that the observations from Fletcher et al. (2017) were made over a year before the images presented in this study, there are several notable similarities: the wave crests have a central latitude of 12°N (compared to 12–17°N in our present study), have a wave number of 16–17 (compared to 18), and are approximately stationary in System III longitude (compared to a slow westward drift rate of 5.44 m/s). Fletcher et al. (2017) also noted that a wave pattern could be seen in near-infrared images taken during that same time period and that the warm crests seen in the thermal infrared observations were anticorrelated with the near-infrared brightness. We also observe the same anticorrelation between the thermal- and near-infrared brightness when we compare the NIRI observations made on 17 May 2017 with 17.65-μm COMICS images taken at a very similar time (see Figure S1 in the supporting information).

If we assume that the near-infrared and thermal infrared data from 2016 and 2017 are all observing the same wave phenomenon, then we can summarize the properties of the crests and troughs as follows. The crests are regions that: (i) sometimes lie above anticyclonic vortices at the main (~0.8-bar) cloud layer, (ii) have low temperatures in the upper troposphere, and (iii) have high-altitude haze in the upper troposphere. The troughs are regions with (i) warm temperatures in the upper troposphere, and (ii) lower-altitude haze in the upper troposphere. These patterns are consistent with vertical oscillations, since upward motion should advect aerosols to higher altitudes and produce colder temperatures in the stably stratified upper troposphere, while downwelling would advect aerosols to lower altitudes and produce adiabatic heating.

Previous observations of thermal wave patterns in Jupiter's NEB have suggested that the most likely classification is a Rossby wave (e.g., Deming et al., 1997; Fletcher et al., 2017; Li et al., 2006), and the analysis of the near-infrared wave observed in this study also supports that conclusion. Rossby waves are slow-moving, planetary-scale waves that arise due to the conservation of absolute vorticity when the flow encounters variations in the planet's Coriolis parameter. The alternating pattern of cyclones and anticyclones that was observed in visible light in March 2017 is characteristic of Rossby waves (e.g., Chandrasekar, 2010). In addition, Rossby waves move slowly westward relative to the mean background flow. Our derived average phase speed of 5.44 m/s west (which is similar to previous measurements from ; Li et al., 2006 and ; Orton et al., 1994) is consistent with this property of Rossby waves, since the background flow is greater than −5.44 m/s at 500 mbar (Li et al., 2006).

Several formation mechanisms have been suggested for these NEB Rossby waves, including forcing from deep Taylor-Proudman columns (Deming et al., 1997), instabilities linked to the vorticity gradient (Achterberg & Flasar, 1996), equatorially produced waves that migrate northward (Fisher et al., 2016), and the effects of convective storms and vortices (e.g., Li et al., 2006). Numerical modeling of the origins of the NEB wave is beyond the scope of this study, but we do note that our observations lend support to the last of these proposed formation mechanisms. As described at the beginning of this section, the majority of the wave crests we observe move westward, with the exception of a single crest which remains fixed in System III longitude during the May–June 2017 time frame. This stationary crest forms the eastern boundary of the wave pattern; new crests form in its vicinity and then slowly drift west from that point. A comparison with visible light images made with the Pic du Midi Observatory (Simon et al., 2018) shows that the stationary wave crest corresponds to an unusually prominent vortex, which is large enough to perturb the boundary of the NEB and the NTZ. Rogers (2017) identifies this vortex as White Spot Z, a long-lived anticyclone. While this vortex remains stationary during the May–June 2017 period when we observe the strongest NEB wave pattern, the ground-based images presented in Simon et al. (2018) show that White Spot Z was drifting eastward in April 2017. The retrievals in section 4.3 also showed that this crest had an unusually high aerosol density. This large, temporarily stationary feature could create an obstacle to the atmospheric flow, leading to the generation of Rossby waves, in a similar manner to a mountain range generating Rossby waves on Earth (Rhines, 2003).

Although large-scale wave patterns have been observed in Jupiter's troposphere since the Voyager flybys (Magalhaes et al., 1989), their appearance varies significantly with time. During some periods of time, there are no discernible waves, and when they are present, a broad range of wave numbers have been observed, including a wave number of 9 in 1979 (Magalhaes et al., 1989), 10–11 in 1987–1988 (Deming et al., 1989; Orton et al., 1994), 13–16 in 2000–2001 (Li et al., 2006; Rogers et al., 2004), and 16–18 in 2016–2017 (Fletcher et al., 2017, this work). It is unclear what drives this temporal variability and how it relates to the formation mechanism of the waves; Fletcher et al. (2017) suggested that the presence of waves in the NEB could be correlated to the periodic expansion events that occur in the belt, where the NEB becomes noticeable broader than normal. This is true for the wave patterns in both 2016 and 2017, as there was a "failed" expansion in 2016, followed by a successful expansion in February–March 2017 (Fletcher et al., 2018). However, Fletcher et al. (2017) conclude that this link cannot be confirmed because published observations are biased towards expansion periods. In the future, by continuing to monitor Jupiter's tropospheric haze patterns and by reanalyzing historical data, we hope to further our understanding of the temporal variability and formation mechanism of Jupiter's NEB wave patterns.

References

Achterberg, R. K., & Flasar, F. M. (1996). Planetary-scale thermal waves in Saturn's upper troposphere. *Icarus*, *119*(2), 350–369.

Borysow, J., Frommhold, L., & Birnbaum, G. (1988). Collision-induced rototranslational absorption spectra of H_2-He pairs at temperatures from 40 to 3000 K. *The Astrophysical Journal*, *326*, 509–515.

Chandrasekar, A. (2010). Basics of atmospheric science, PHI.

Deming, D., Mumma, M. J., Espenak, F., Jennings, D. E., Kostiuk, T., Wiedemann, G., et al. (1989). A search for *p*-mode oscillations of Jupiter—Serendipitous observations of nonacoustic thermal wave structure. *The Astrophysical Journal*, *343*, 456–467.

Deming, D., Reuter, D., Jennings, D., Bjoraker, G., McCabe, G., Fast, K., & Wiedemann, G. (1997). Observations and analysis of longitudinal thermal waves on Jupiter. *Icarus*, *126*(2), 301–312.

Fisher, B. M., Orton, G. S., Liu, J., Schneider, T., Ressler, M. E., & Hoffman, W. F. (2016). The organization of Jupiter's upper tropospheric temperature structure and its evolution, 1996–1997. *Icarus*, *280*, 268–277.

Fletcher, L. N., Melin, H., Adriani, A., Simon, A. A., Sanchez-Lavega, A., Donnelly, P. T., et al. (2018). Jupiter's mesoscale waves observed at 5 m by ground-based observations and Juno JIRAM. *The Astronomical Journal*, *156*(2), 67.

Fletcher, L. N., Orton, G., Rogers, J., Simon-Miller, A., De Pater, I., Wong, M., et al. (2011). Jovian temperature and cloud variability during the 2009–2010 fade of the South Equatorial Belt. *Icarus*, *213*(2), 564–580.

Fletcher, L. N., Orton, G. S., Sinclair, J. A., Donnelly, P., Melin, H., Rogers, J. H., et al. (2017). Jupiter's North Equatorial Belt, expansion and thermal wave activity ahead of Juno's arrival. *Geophysical Research Letters*, *44*, 7140–7148. https://doi.org/10.1002/2017GL073383

Fletcher, L., Orton, G., Teanby, N., & Irwin, P. (2009). Phosphine on Jupiter and Saturn from Cassini/CIRS. *Icarus*, *202*(2), 543–564.

Gordon, I. E., Rothman, L. S., Hill, C., Kochanov, R. V., Tan, Y., Bernath, P. F., et al. (2017). The HITRAN2016 molecular spectroscopic database. *Journal of Quantitative Spectroscopy and Radiative Transfer*, *203*, 3–69.

Hatzes, A., Wenkert, D. D., Ingersoll, A. P., & Danielson, G. E. (1981). Oscillations and velocity structure of a long-lived cyclonic spot. *Journal of Geophysical Research*, *86*(A10), 8745–8749.

Hodapp, K. W., Jensen, J. B., Irwin, E. M., Yamada, H., Chung, R., Fletcher, K., et al. (2003). The Gemini near-infrared imager (NIRI). *Publications of the Astronomical Society of the Pacific*, *115*(814), 1388.

Hueso, R., Sánchez-Lavega, A., & Guillot, T. (2002). A model for large-scale convective storms in Jupiter. *Journal of Geophysical Research*, *107*(E10), 5075. https://doi.org/10.1029/2001JE001839

Acknowledgments

This paper is based on observations obtained at the Gemini Observatory and processed using the Gemini IRAF package, which is operated by the Association of Universities for Research in Astronomy, Inc., under a cooperative agreement with the NSF on behalf of the Gemini partnership: the National Science Foundation (United States), the National Research Council (Canada), CONICYT (Chile), Ministerio de Ciencia, Tecnología e Innovación Productiva (Argentina), Ministério da Ciência, Tecnologia e Inovação (Brazil), and Korea Astronomy and Space Science Institute (Republic of Korea). The data are available from the Gemini Observatory Archive, and the program identification numbers are GN-2016B-Q-52, GN-2017A-Q-10, and GN-2018A-Q-108. The authors wish to recognize and acknowledge the very significant cultural role and reverence that the summit of Maunakea has always had within the indigenous Hawaiian community. We are most fortunate to have the opportunity to conduct observations from this mountain. The supporting information made use of data collected at Subaru Telescope, which is operated by the National Astronomical Observatory of Japan. The data are available from the Subaru-Mitaka Okayama-Kiso Archive System. The supporting information also used data acquired from the NASA/ESA HST Space Telescope, associated with OPAL program (PI: Simon, GO13937), and archived by the Space Telescope Science Institute, which is operated by the Association of Universities for Research in Astronomy, Inc., under NASA contract NAS 5-26555. All maps are available at this website (https://doi.org/10.17909/T9G593). The research was carried out in part at the Jet Propulsion Laboratory, California Institute of Technology, under a contract with the National Aeronautics and Space Administration. Giles was supported by the NASA Postdoctoral Program, and Orton, Sinclair, and Tabataba-Vakili were supported by grants from NASA to the Jet Propulsion Laboratory/California Institute of Technology. Irwin was supported by the UK Science and Technology Facilities Council.

Irwin, P., Teanby, N., de Kok, R., Fletcher, L., Howett, C., Tsang, C., et al. (2008). The NEMESIS planetary atmosphere radiative transfer and retrieval tool. *Journal of Quantitative Spectroscopy and Radiative Transfer*, *109*(6), 1136–1150.

Irwin, P., Weir, A., Smith, S., Taylor, F., Lambert, A., Calcutt, S., et al. (1998). Cloud structure and atmospheric composition of Jupiter retrieved from Galileo near-infrared mapping spectrometer real-time spectra. *Journal of Geophysical Research*, *103*(E10), 23,001–23,021.

Johnson, P. E., Morales-Juberías, R., Simon, A., Gaulme, P., Wong, M. H., & Cosentino, R. G. (2018). Longitudinal variability in Jupiter's zonal winds derived from multi-wavelength HST observations. *Planetary and Space Science*, *155*, 2–11.

Kataza, H., Okamoto, Y., Takubo, S., Onaka, T., Sako, S., Nakamura, K., et al. (2000). COMICS: The cooled mid-infrared camera and spectrometer for the Subaru telescope. In S. Ikeuchi, J. Hearnshaw, & T. Hanawa (Eds.), *Optical and IR Telescope Instrumentation and Detectors* (Vol. 4008, pp. 1144–1153). Tokyo: International Society for Optics and Photonics.

Lacis, A. A., & Oinas, V. (1991). A description of the correlated k distribution method for modeling nongray gaseous absorption, thermal emission, and multiple scattering in vertically inhomogeneous atmospheres. *Journal of Geophysical Research*, *96*(D5), 9027–9063.

Leggett, S., Currie, M., Varricatt, W., Hawarden, T., Adamson, A., Buckle, J., et al. (2006). JHK, observations of faint standard stars in the Mauna Kea Observatories near-infrared photometric system. *Monthly Notices of the Royal Astronomical Society*, *373*(2), 781–792.

Li, L., Ingersoll, A. P., Vasavada, A. R., Simon-Miller, A. A., Achterberg, R. K., Ewald, S. P., et al. (2006). Waves in Jupiter's atmosphere observed by the Cassini ISS and CIRS instruments. *Icarus*, *185*(2), 416–429.

Limaye, S. S. (1986). Jupiter: New estimates of the mean zonal flow at the cloud level. *Icarus*, *65*(2-3), 335–352.

Magalhaes, J., Weir, A., Conrath, B., Gierasch, P., & Leroy, S. (1989). Slowly moving thermal features on Jupiter. *Nature*, *337*(6206), 444.

Martonchik, J. V., Orton, G. S., & Appleby, J. F. (1984). Optical properties of NH_3 ice from the far infrared to the near ultraviolet. *Applied optics*, *23*(4), 541–547.

Minnaert, M. (1941). The reciprocity principle in lunar photometry. *The Astrophysical Journal*, *93*, 403–410.

Niemann, H., Atreya, S., Carignan, G., Donahue, T., Haberman, J., Harpold, D., et al. (1998). The composition of the Jovian atmosphere as determined by the Galileo probe mass spectrometer. *Journal of Geophysical Research*, *103*(E10), 22,831–22,845.

Nixon, C., Achterberg, R., Conrath, B., Irwin, P., Teanby, N., Fouchet, T., et al. (2007). Meridional variations of C_2H_2 and C_2H_6 in Jupiter's atmosphere from Cassini CIRS infrared spectra. *Icarus*, *188*(1), 47–71.

Orton, G. S., Friedson, A. J., Yanamandra-Fisher, P. A., Caldwell, J., Hammel, H. B., Baines, K. H., et al. (1994). Spatial organization and time dependence of Jupiter's tropospheric temperatures, 1980–1993. *Science*, *265*(5172), 625–631.

Orton, G. S., Gustafsson, M., Burgdorf, M., & Meadows, V. (2007). Revised ab initio models for H_2-H_2 collision-induced absorption at low temperatures. *Icarus*, *189*(2), 544–549.

Rhines, P. B. (2003). *Encyclopaedia of atmospheric sciences, chap. Rossby Waves*. Oxford: Academic Press Oxford.

Rogers, J. H. (1995). *The giant planet Jupiter* (Vol. 6). Cambridge, UK: Cambridge University Press.

Rogers, J. (2017). Jupiter in 2016–2017, British Astronomical Association.

Rogers, J. H., Akutsu, T., & Orton, G. S. (2004). Jupiter in 2000/2001. Part II: Infrared and ultraviolet wavelengths. *Journal of the British Astronomical Association*, *114*, 313.

Simon, A. A., Hueso, R., Iñurrigarro, P., Sánchez-Lavega, A., Morales-Juberías, R., Cosentino, R., et al. (2018). A new, long-lived, Jupiter mesoscale wave observed at visible wavelengths. *The Astronomical Journal*, *156*(2), 79.

Sromovsky, L., Collard, A., Fry, P., Orton, G., Lemmon, M., Tomasko, M., & Freedman, R. (1998). Galileo probe measurements of thermal and solar radiation fluxes in the Jovian atmosphere. *Journal of Geophysical Research*, *103*(E10), 22,929–22,977.

Tollefson, J., Wong, M. H., de Pater, I., Simon, A. A., Orton, G. S., Rogers, J. H., et al. (2017). Changes in Jupiter's zonal wind profile preceding and during the Juno mission. *Icarus*, *296*, 163–178.

Wong, M. H., Marchis, F., Marchetti, E., Amicom, P., Tordo, S., Bouy, H., & de Pater, I. (2008). A shift in Jupiter's equatorial haze distribution imaged with the multi-conjugate adaptive optics demonstrator at the VLT. AAS/DPS Meeting Abstracts (Vol. 40).